

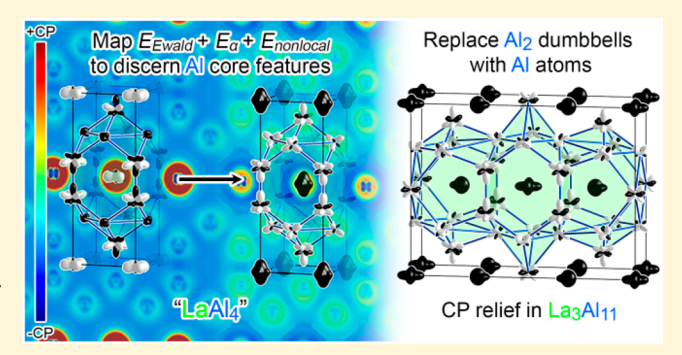
Discerning Chemical Pressure amidst Weak Potentials: Vibrational Modes and Dumbbell/Atom Substitution in Intermetallic Aluminides

Katerina P. Hilleke and Daniel C. Fredrickson*

Department of Chemistry, University of Wisconsin—Madison, 1101 University Avenue, Madison, Wisconsin 53706, United States

Supporting Information

ABSTRACT: The space requirements of atoms are generally regarded as key constraints in the structures, reactivity, and physical properties of chemical systems. However, the empirical nature of such considerations renders the elucidation of these size effects with first-principles calculations challenging. DFT-chemical pressure (DFT-CP) analysis, in which the output of DFT calculations is used to construct maps of the local pressures acting between atoms due to lattice constraints, is one productive approach to extracting the role of atomic size in the crystal structures of materials. While in principle this method should be applicable to any system for which DFT is deemed an appropriate



treatment, so far it has worked most successfully when semicore electrons are included in the valence set of each atom to supply an explicit repulsive response to compression. In this Article, we address this limiting factor, using as model systems intermetallics based on aluminum, a key component in many structurally interesting phases that is not amenable to modeling with a semicore pseudopotential. Beginning with the Laves phase CaAl2, we illustrate the difficulties of creating a CP scheme that reflects the compound's phonon band structure with the original method due to minimal core responses on the Al atoms. These deficiencies are resolved through a spatial mapping of three energetic terms that were previously treated as homogeneous background effects: the Ewald, Ea and nonlocal pseudopotential components. When charge transfer is factored into the integration scheme, CP schemes consistent with the phonon band structure are obtainable for CaAl2, regardless of whether Ca is modeled with a semicore or valence-only pseudopotential. Finally, we demonstrate the utility of the revised method through its application to the La₃Al₁₁ structure, which is shown to soothe CPs that would be encountered in a hypothetical BaAl₄-type parent phase through the substitution of selected Al₂ pairs with single Al atoms. La₃Al₁₁ then emerges as an example of a more general phenomenon, CP-driven substitutions of simple motifs.

1. INTRODUCTION

One need only glance through the various definitions of atomic radii in common use to see both the vital role that atomic size plays in our understanding of chemical systems and the challenges it poses. Covalent, ionic, metallic, and van der Waals radii are frequently referred to in discussions of interatomic distances, while alternative definitions have been derived from such diverse sources as the maxima in radial density distributions,² the sphere radii that enclose a specific fraction of the electron density,³ or even pseudopotential parameters.⁴ The issue of defining atomic size is compounded by the qualifiers (oxidation state, bond order, hybridization, coordination number) that often accompany these radii. This wide range of radii for any given element emphasizes that an atom's size is highly dependent on its electronic context.

The connection between size and electronic structure would seem to make quantum mechanical calculations a valuable resource for understanding the spatial requirements of atoms in any given structure. Indeed, several schemes have been devised for determining the volume occupied by an atom from a compound's electron density, such as the quantum theory of atoms in molecules^{5,6} and the iterative Hirshfeld⁷⁻⁹ or stockholder atom approaches. 10 However, it remains challenging to extract information about how the strain in atomic packing due to size constraints influences the structure and properties of a molecule or material from theoretical calculations alone. Establishing such a method with these capabilities is particularly important for intermetallic phases. In this broad family of solid state compounds, atomic size is empirically known to play a key role in defining the stability ranges of the diverse structures encountered, 11,12 and such effects are frequently invoked when structural phenomena are explained here in a manner analogous to that of sterics in organic chemistry. ^{13–21} These discussions would benefit from theoretical tools that analyze how the atomic size factor specifically directs these structural phenomena.

Recently, we demonstrated that, as a simple implementation of the quantum mechanical stress density formalism, 22-26 the

Received: July 31, 2018 Revised: September 18, 2018 Published: October 2, 2018

chemical pressure (CP) method can illuminate the interaction between atomic size and electronic structure. This approach has allowed the elucidation of a number of structural phenomena in intermetallic phases, such as the deletion of atomic layers to create superstructures, the formation of local icosahedral ordering in quasicrystal approximants, the substitution of atoms and dumbbells, the appearance of incommensurately spaced layers of atoms, the appearance of incommensurately spaced layers of atoms, the appearance of incompatible domains. The have also found that the CP schemes of a material can provide a window into its vibrational modes, where atoms with quadrupolar CP distributions are subject to soft atomic motions along preferred directions highlighting potential paths for phase transitions or modulations.

In principle, this approach is applicable to all systems in which DFT is considered a reasonable treatment of the electronic structure. In practice, however, the method relies on the interpretation of maps in which atomic core regions with positive pressure stand out against a shallower background of negative pressure. Depending on the pseudopotentials used, the pressure magnitudes in the core regions can vary widely, and the CP method has been most useful in cases where combinations of pseudopotentials can be chosen such that the core responses on different elements are of comparable magnitudes. Unfortunately, this condition excludes a large fraction of intermetallic chemistry, as the available pseudopotentials for certain staple elements, such as Al and Si, are so soft that the current implementation of the CP approach shows only minimal activity in their core regions.

In this Article, we will introduce improvements to the DFT-CP approach that allow insights into systems involving such soft pseudopotentials. Our first model system will be the compound CaAl₂ (Figure 1, left), a MgCu₂-type phase whose

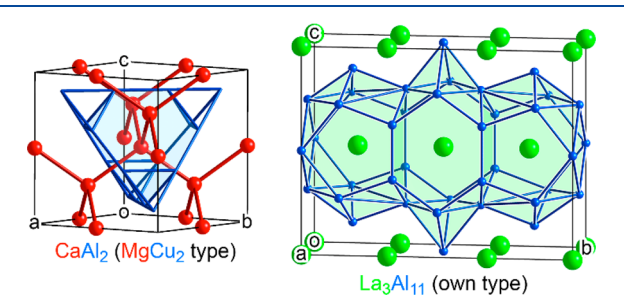


Figure 1. The crystal structures of CaAl₂ and La₃Al₁₁, model systems to be used in the CP method development of this work.

valence electron density³⁸ and electron localization function (ELF)³⁹ have been previously analyzed, and whose ternary variants have been extensively studied in efforts to understand the structural preferences within Laves phases.^{40–44} Using the original CP method, we will see negative Al–Al pressures emerge for this compound that cannot be reconciled with the phonon band structure of the material, in contrast to results previously obtained for its Pd analogue, CaPd₂.³¹ We will then reexamine the energetic terms included in the CP maps, improving the treatment of contributions added homogeneously to the map in the original method. After demonstrating the revised method's ability to account for the most striking features of CaAl₂'s phonon band structure, we will apply it to explaining the more complex structure of La₃Al₁₁ (Figure 1, right)⁴⁵ where Al–Al repulsion will be seen to play a decisive role.

2. COMPUTATIONAL DETAILS

DFT-CP calculations were performed on CaAl₂, CaPd₂, LaAl₄ (in the BaAl₄-type), and La₃Al₁₁. First, non-spin-polarized LDA-DFT geometry optimizations were carried out using the ABINIT software package $^{46-49}$ with Hartwigsen—Goedecker—Hutter norm-conversing pseudopotentials. Following the determination of the LDA-DFT optimized geometry, calculations were performed at the equilibrium geometry as well as at isotropically expanded and contracted volumes ($\pm 0.5\%$) in preparation for the chemical pressure analysis. Kinetic energy and electron densities as well as local components of the Kohn—Sham potential were mapped over a 3D voxel grid. Further details, including the k-point grids and energy cutoffs used in the calculations, may be found in the Supporting Information

The phonon band structures of CaPd₂, CaAl₂, and LaAl₄ were calculated with ABINIT using the linear-response method. S1,52 Beginning from a wavefunction file generated for the optimized geometry with a Γ -centered k-point grid, atomic linear responses in all three directions were determined via non-self-consistent calculations at individual q-points, with one q-point for each k-point in the reference calculation. From these linear response calculations, the ABINIT utilities mrgddb and anaddb were used to determine force constants for all atoms. Phonon modes were visualized using Figuretool2, an inhouse MATLAB application.

In order to determine Bader charges for use in the CP analysis, geometry optimizations were carried out in the Vienna Ab initio Simulation Package (VASP)^{53,54} using PAW-GGA pseudopotentials^{55,56} in the high precision mode. The program Bader^{57–59} was used to extract atomic charges from the charge density files output by VASP.⁶⁰ The atomic pseudopotentials engine (APE)⁶¹ was then used to generate radial electron density profiles corresponding to a range of charges from 0 to 100% of the Bader charge as applicable for use in the Hirshfeld-inspired integration scheme.

Prior to carrying out the generation and integration of the chemical pressure maps, the nonlocal pseudopotential energy was mapped for the expanded and contracted geometries from the ABINIT calculations using the new program CPnonlocal, which produces as output XSF files containing the mapped nonlocal energy. These were read into the updated Chemical Pressure Software Package (CPpackage2, available on the Fredrickson group Web site at http://www.chem.wisc.edu/~danny/software). CP maps were generated with core unwarping using tricubic interpolation. For the creation of CP schemes, unit cells were partitioned into contact volumes between pairs of atoms using the Hirshfeld-inspired scheme. Following averaging of the CP contained within these contact volumes, the resulting interatomic pressure contributions were projected onto atom-centered spherical harmonics ($l \le 4$), and the results were visualized with Figuretool2.

3. RESULTS AND DISCUSSION

3.1. Energy Partitioning in the CP Method. Over the course of this Article, we will introduce revisions to the CP approach to make it more amenable to atoms modeled with soft pseudopotentials for which interatomic interactions do not appear to elicit strong repulsive core responses. Let us begin with a brief review of the current CP map generation scheme, with particular attention to the energetic terms that are most likely tied to pseudopotential dependence.

In the production of CP maps, the first step is to create an energy density distribution for a structure based on the total DFT energy:

$$E_{\rm DFT} = \iiint_{\rm cell} \left[\frac{1}{2} \sum_{j} o_{j} |\nabla \psi_{j}|^{2} + (V_{\rm local} + V_{\rm Hartree} + \varepsilon_{\rm xc}) \rho(\vec{r}) \right] d\tau$$

$$+ E_{\rm nonlocal} + E_{\rm Ewald} + E_{\alpha}$$
(1)

where o_j is the occupation of the one-electron eigenfunction ψ_{j} . This expression can be partitioned into two sections. The upper line corresponds to a mappable portion. The energy density corresponding to the integrand here can be constructed on a grid of voxels (the three-dimensional analogues of pixels), using the kinetic energy density, electron density, and components of the Kohn–Sham potential (minus the divergent Fourier components at the origin of reciprocal space, $\mathbf{G} = \mathbf{0}$) provided by the output of a DFT calculation.

The lower line of eq 1, however, contains terms that are not easily expressed as a simple integral over 3D space: $E_{\rm Ewald} + E_{\alpha}$ corresponds to the potential energy of a homogeneous electron gas combined with the pseudopotential ion cores, merging the G=0 components of the electron–electron and electron—ion potential energies and the internuclear repulsion in a nondivergent manner. The third nonmappable term, $E_{\rm nonlocab}$ represents the nonlocal component to the pseudopotential-electron interaction energy. Until now, we have simply treated these as homogeneous contributions to the energy map.

With these spatially resolved DFT energy maps in hand, we can derive a *chemical pressure* (CP) function by determining how the energy contained in each voxel changes as the structure is slightly expanded and contracted. The simplest expression for this calculation is given by

$$P_n = -\frac{\partial E_n}{\partial V_{\text{voxel}}} \approx -\frac{E_n^+ - E_n^-}{V_{\text{voxel}}^+ - V_{\text{voxel}}^-}$$
(2)

with E_n^+ and E_n^- being the contributions to the DFT total energy from voxel n in the expanded (+) and contracted (-) structures, respectively. A somewhat more sophisticated approach is given by the core-unwarping procedure, in which an interpolation is used to reduce the motions of the grid point positions relative to the atomic core regions between the expanded and contracted structures.³⁰

For a metallic system, a CP map generally consists of a bath of negative pressure spread across the interstitial regions of the unit cell with positive CP features being centered on atomic cores, as illustrated in Figure 2a. Finer features may be discerned within the positive core response regions, distorting them from spherical symmetry, or in the negative background of the CP map.

Determining the net character of any particular interatomic interaction, i.e., its magnitude and whether it is attractive or repulsive, requires us to integrate the positive CP core features and negative CP interstitial space corresponding to that interaction. To do this, we divide the unit cell volume into contact volumes (following one of numerous possible schemes) that represent the regions of space assigned to the interactions for pairs of atoms. The individual chemical pressures for the voxels within a particular contact volume are then averaged to give a single chemical pressure value for the contact.

For a CP analysis to be successful, then, each contact volume must enclose the proper balance of positive and negative CP to accurately represent the spatial preferences of each atom. In

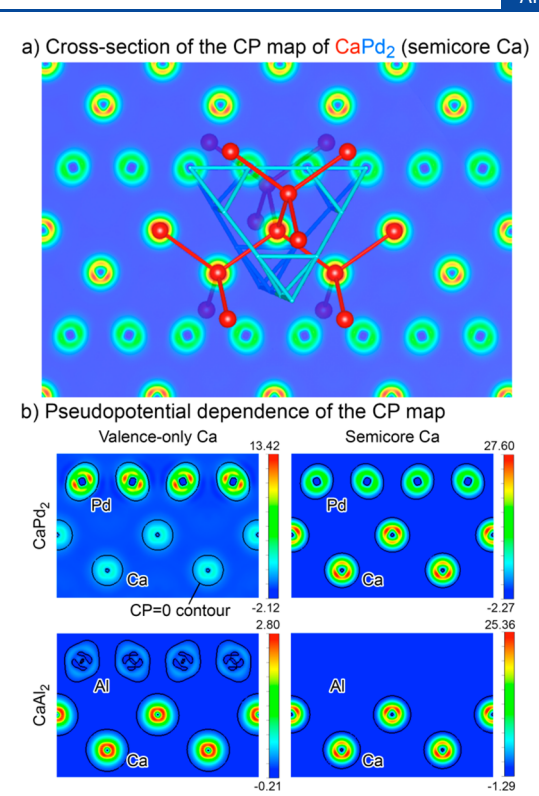


Figure 2. Pseudopotential dependence of core responses in the original CP method. (a) Slice through the CP map of $MgCu_2$ -type $CaPd_2$. (b) CP maps for $CaAl_2$ and $CaPd_2$ with semicore or valence-only pseudopotentials. Contours at CP=0.0 are overlaid in black. Pressures on the color bar labels are given in TPa.

our prior work, we developed a scheme for constructing contact volumes inspired by the Hirshfeld scheme⁶³ for assigning atomic charges.³⁰ In the Hirshfeld charge scheme, a hypothetical pro-density is first created from a superposition of free atom electron densities. The ground state electron density of a structure at each point is then divided between atoms according to their relative contributions to the pro-density at that point. This can be simply generalized to dividing space into contact volumes for the CP method: one just assigns a voxel to the pair of atoms that contribute the most to the prodensity at that voxel. Using this Hirshfeld-inspired scheme, we have been able to explain a variety of structural phenomena and highlight the connection between the presence of soft phonon modes and structural features, particularly when free atom electron densities are replaced with those of anions or cations to account for the ionicity of a compound. 31 We are in the process of developing a new method that circumvents the use of free-atom reference states and adjustable ion charges, but for now we will continue to use this Hirshfeld-inspired approach.

Here, we focus instead on difficulties that can arise from the features of the CP maps themselves, particularly in cases where atoms of very dissimilar elements are combined. To illustrate this issue, we show in Figure 2 a series of CP maps for two compounds: the MgCu₂-type phases CaAl₂ and CaPd₂. The majority elements, Al and Pd, have pseudopotentials of quite different character. Al is often cited as an exemplar of nearly free electron character; ⁶⁴ as such, its pseudopotential is very soft. Pd, however, with its localized 4d¹⁰ subshell, is modeled by a much harder pseudopotential. This difference is evident in the CP maps, where the Pd atoms are decorated by intense

rings of positive CP, while the corresponding features for the Al atoms are barely perceptible.

The CP features of the Ca atoms present in both compounds can also prove illuminating in this comparison. For CaPd₂ (Figure 2b, top row), a semicore Ca pseudopotential is needed for the Ca core response to stand out against the Pd atoms' features. In CaAl₂ (Figure 2b, bottom row), the use of a semicore pseudopotential on Ca completely drowns out any Al core response, and even a valence-only pseudopotential confers a much stronger response on the Ca atoms than is seen around the Al ones. These disparities have consequences for the integrated CP schemes: positive CP cannot arise between two atoms whose CP core responses are nigh undetectable against the negative CP background. Thus, the CP method has worked best for combinations of elements with similar core properties, which is an unfortunately narrow range of elements.

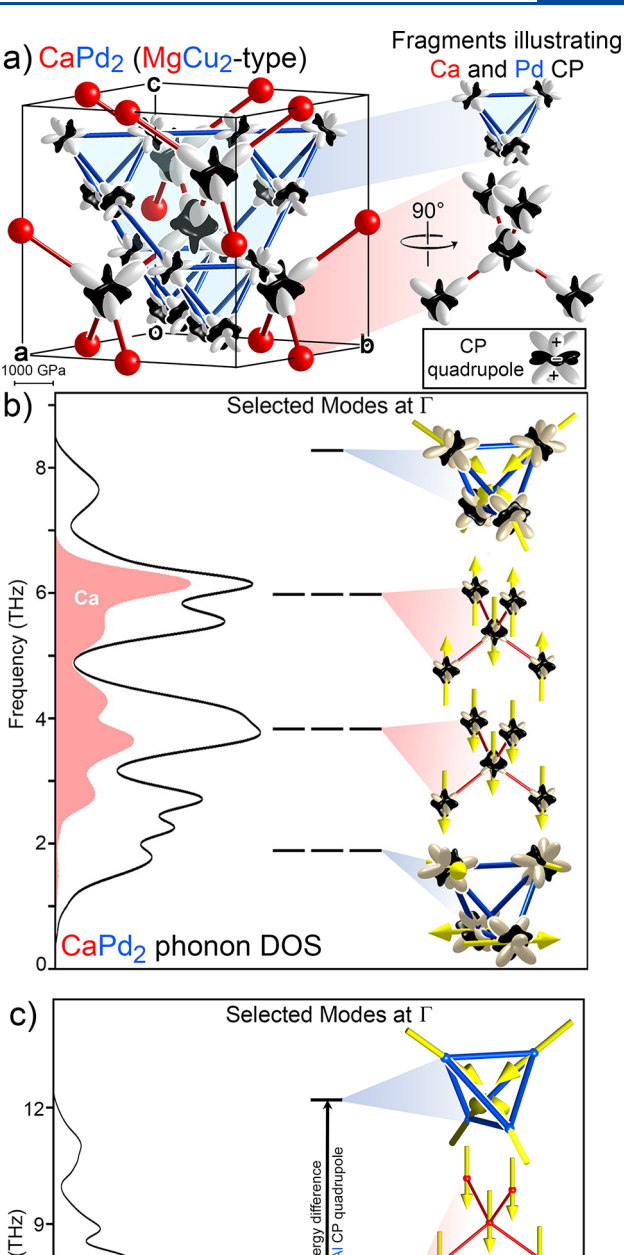
In the following sections, we will work to address this limitation, allowing the CP method to be used freely for a variety of elemental combinations. Of particular importance will be the nonmappable energy terms: E_{Ewald} , E_{co} and E_{nonlocal} .

3.2. Vibrational Modes: CaPd₂ vs CaAl₂. In our development of a revised CP map formalism, it will be very helpful to have a clear view of what a correct CP scheme should look like. As we saw in our previous analysis of CaPd₂, ³¹ the phonon band structure of a material can provide a guide to calibrating the CP method. In Figure 3a, we revisit these results, beginning with the integrated CP scheme of CaPd₂. Here, the CPs experienced by each atom are illustrated with radial plots using our standard convention: the length of a CP lobe emanating from an atom is proportional to the sums of the pressure contributions along that direction (after averaging within contact volumes). The color of the lobes indicates the sign of the CP: negative CP is indicated by black (by analogy to black holes) and highlights contacts that would be stabilized by the contraction of the structure. Positive CP, conversely, is displayed as white, indicating contacts that would be stabilized by expansion.

The distribution of white and black lobes throughout the CP scheme of CaPd₂ highlights a fundamental tension within the structure. Black CP features point from the atoms into the interstitial spaces between the Ca atoms (arranged in a diamond network) and the Pd atoms (arrayed in tetrahedra that share corners to form a separate diamond network). The Ca–Pd contacts are then overly long, and call for the structure to shrink. However, the structure is prevented from contracting by positive CPs (white lobes) along the Ca–Ca and Pd–Pd contacts. The homoatomic contacts are already too short and push toward expansion of the structure.

As we described earlier in a mode-by-mode analysis, 31 these CP features are in close accord with CaPd₂'s phonon band structure. In Figure 3b, we summarize these results with a phonon density of states (DOS) distribution plotted alongside selected vibrational modes at the Γ point. Here, the stiffest atomic motions tend to run along positive CPs, where contraction of interatomic distances is expected to face an exponentially growing energetic cost. The softer atomic motions, meanwhile, occur along directions of negative CP, where the contraction of distances is favorable and stretching them leads to interactions whose energies asymptotically approach zero (i.e., the local curvature of the interatomic interaction energy with respect to distance is negative).

A particularly important feature in this scheme is the presence of a CP quadrupole on each Pd atom (Figure 3a) in



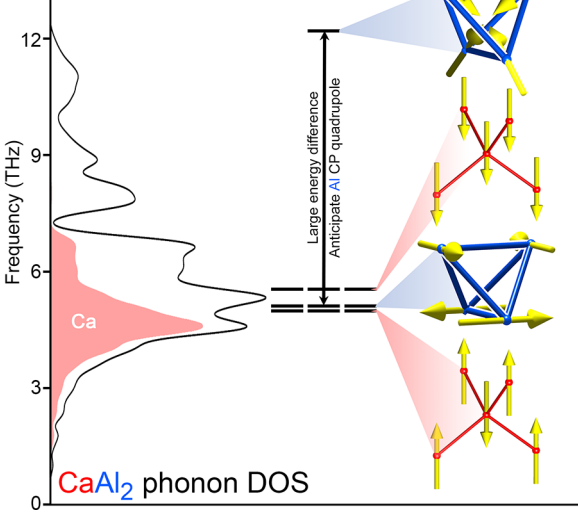


Figure 3. Calibration of CP schemes against phonon frequencies. (a) CP scheme of CaPd₂. CP plots for the Ca atoms on the cell edges are omitted for clarity. (b) Phonon density of states (DOS) calculated for CaPd₂, with selected modes at the Γ point plotted in the context of the CP scheme. (c) Phonon DOS of CaAl₂, and selected modes at the Γ point used for calibration of its CP scheme. (b) is adapted from ref 31 with the permission of the American Chemical Society.

which the positive and negative CP features on a single atom are arranged perpendicular to each other, creating strong

anisotropy. Indeed, the Pd atoms dominate both the highest and lowest frequency optical modes at the Γ point, corresponding respectively to motions parallel and perpendicular to the positive axis of the CP quadrupole. With respect to the Ca atoms, the lack of a CP quadrupole is reflected in the smaller gap separating high-frequency from low-frequency modes.

How do these features change when we move to CaAl₂, a compound with the same structure type but different elements? In Figure 3c, we show the phonon DOS of CaAl₂, as well as the analogous modes at the Γ point to those highlighted for CaPd2 in Figure 3b. Two of these modes involve motions of the Al atoms, and as in CaPd2, the high frequency one corresponds to the contraction and expansion of the Al/Pd tetrahedra. The other Al-based mode is among the lowest frequency optical modes, corresponding to concerted tilting of the tetrahedra that largely preserve the near-neighbor Al-Al distances. Just as for their CaPd2 counterparts, the frequency difference between these two Al-based modes spans nearly the whole range of optical modes. Here, though, the range of frequencies is larger than in CaPd2, as may be expected from Al's smaller atomic mass. The large energy splitting between these two modes, which was also present in CaPd₂, is suggestive of the presence of CP quadrupoles on the Al atoms, oriented so that the Al–Al contacts display positive

By contrast, the Ca vibrations are distributed differently across the phonon density of states (DOS) of CaAl₂ than in CaPd₂, as can be seen in the projected DOS curves (pink in Figures 3b,c). For CaPd₂, the Ca projected DOS is split across a deep minimum at about 5 THz, roughly at the center of the frequency range. The two Ca-based phonon modes at Γ in Figure 3b straddle this DOS minimum, with the lower and upper modes corresponding to in-phase and out-of-phase motions of the Ca atoms. In CaAl₂, the Ca projected DOS is concentrated in the lower half of the phonon band structure, below the most prominent DOS minimum. Perhaps more strikingly, the order of the modes with in-phase and out-of-phase motions of the Ca atoms has become reversed.

The potential origins of these trends become clearer when we consider the role that the atomic mass difference between Pd and Al plays in these modes.⁶⁵ As is shown in the Supporting Information, the out-of-phase Ca vibrational mode involves only motions of the Ca atoms; the Pd or Al atoms remain fixed in place due to symmetry constraints. The relative frequencies of this mode in CaAl2 and CaPd2 can then be used to directly compare the stiffness of the Ca atom motions in the two structures. Its lower frequency in CaAl₂ than in CaPd₂ (5.1 vs 6.0 THz) suggests that the Ca atoms in CaAl2 have an effectively looser coordination environment. The in-phase Ca mode, however, involves motion of both the Ca and Al/Pd atoms as the two sublattices slide relative to each other. As such, the frequencies of this mode will be influenced by the atomic mass of the Al or Pd. As Al atoms are significantly lighter than Ca and Pd, the in-phase mode appears in CaAl2 at higher frequencies than it does in CaPd₂ (5.6 vs 3.8 THz), allowing for the frequencies of the in-phase and out-of-phase motions to be inverted.

In our earlier analysis of $CaPd_2$, we attributed the higher frequency of the out-of-phase Ca-based mode to positive Ca-Ca CP lobes that appear when the charges of the Ca and Pd atoms used in the Hirshfeld-inspired contact volume construction are set to ca. 50% of those obtained in a Bader

analysis. However, the comparison with CaAl₂ makes it clear that the lower frequency of the in-phase mode in CaPd₂ could also be explained in terms of the heavier mass of the Pd atoms that are also involved in the mode. In this way, the influence of the atomic mass difference between Ca and Al or Pd in the relative frequencies of the Ca-based modes makes it more difficult to derive from them specific expectations for the CP scheme. The Al/Pd-based modes in Figure 3b,c, by contrast, involve exclusively motions of those atoms, making their correlations to the CP scheme cleaner. The Al atoms are clearly expected to show CP quadrupoles whose positive poles align with the Al–Al interactions.

Upon carrying out a CP analysis on CaAl₂, however, the difficulties of deriving CP schemes for Al-containing intermetallics become apparent. In Figure 4, we illustrate CP schemes for CaAl₂ using both semicore and valence-only Ca pseudopotentials, and with a range of ionicities used in the Hirshfeld-inspired integration scheme. In each case, the Al atoms exhibit black negative CP lobes pointing toward each of their six Al neighbors. For most of the schemes, the Al atoms

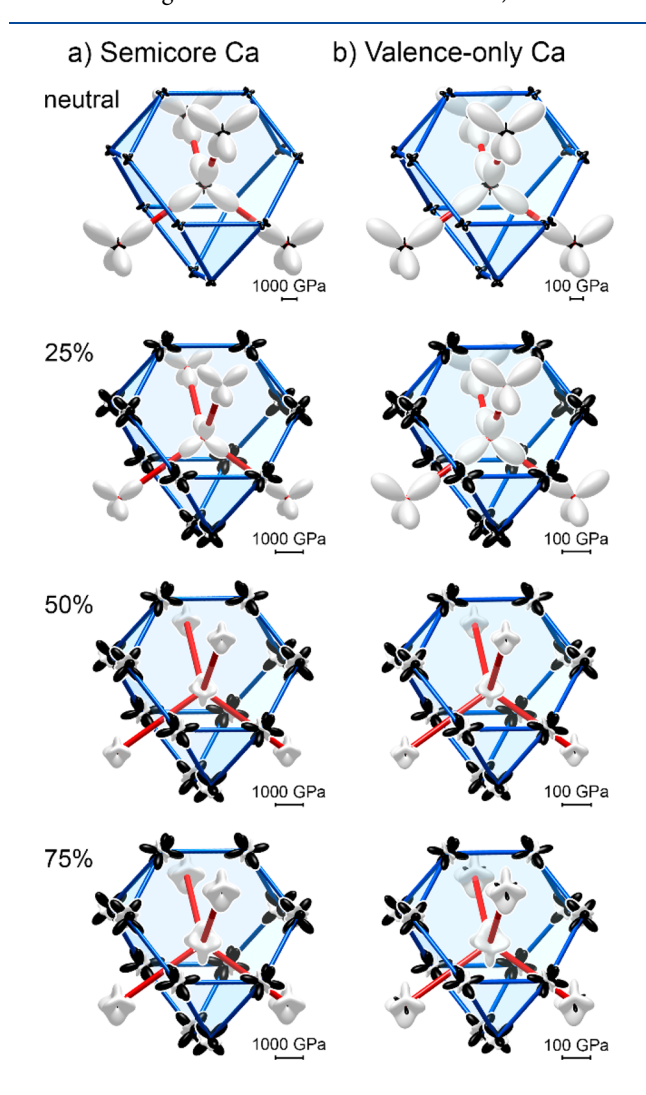


Figure 4. CP schemes of CaAl₂ calculated with (a) semicore and (b) valence-only Ca pseudopotentials and assuming different charges during the integration of the CP maps (expressed as percentages of the Bader charges). Negative Al–Al CPs occur in all cases, in contradiction to the expectations derived from the phonon band structure.

also display smaller positive CP features directed toward the Ca atoms, nearly the opposite of the CP quadrupole anticipated by the phonon band structure. The concentration of the negative CP on the Al atoms results in largely positive CPs on the Ca, which can be directed toward the other Ca atoms or toward the Al, depending on the ionicity parameter.

These difficulties can be simply understood from the features of the CP maps described above. The Al atoms in these maps display only faint core responses (Figure 2). As the contact volumes between Al atoms have no significant source of positive CP, the integrated CP schemes yield no positive Al–Al CPs. In CaPd₂, where the agreement between the CP scheme and band structure is much stronger, the Pd atoms show strong positive core responses even when combined with semicore Ca pseudopotentials.

3.3. Revised Mapping Scheme. It thus appears that the energetic terms leading to stiffness in the Al–Al interactions evident in the phonon band structure are not being spatially mapped correctly in the CP analysis. Particular suspects here are terms treated as homogeneous background effects: the Ewald energy, the E_{α} component, and the nonlocal pseudopotential energy. We will now examine these terms in detail to determine how their homogeneous mapping fails to capture some key interatomic repulsions, and how they can be spatially resolved.

3.3.1. Ewald Energy. The Ewald energy $(E_{\rm Ewald})$ corresponds to the electrostatic energy for a neutral system consisting of an array of point charges (corresponding to the ion cores) and a homogeneous electron gas. It is computed using Ewald summation, in which the Coulomb interactions are divided into short-range and long-range energetic components that can be efficiently computed in real and Fourier space, respectively.

While this energy term contains both an attractive (ion core—electron) and a repulsive (ion core—ion core, electron—electron) component, for intermetallic phases the attractive portion dominates to the point that the $E_{\rm Ewald}$ is usually among the largest contributors of negative pressure to the CP map. Mapping it homogeneously has the advantage of highlighting with negative pressure regions of space that are sparsely populated, indicating how the atomic packing in these regions is inefficient. However, as we saw above, this negative background can become overwhelming for atoms modeled with softer pseudopotentials.

An examination of how the $E_{\rm Ewald}$ is calculated can lead us to ways of mitigating this issue. Following Martin, ⁶² the $E_{\rm Ewald}$ for a system of ions n and m with charges $Z_n^{\rm ion}$, unit cell volume $V_{\rm cell}$, and interatomic vectors $\boldsymbol{\tau}_{n,m}$ is given (in atomic units) by

$$E_{\text{Ewald}} = \sum_{n,m} \frac{Z_n^{\text{ion}} Z_m^{\text{ion}}}{2} \left[\sum_{\mathbf{T}} \frac{\text{erfc}(\eta | \boldsymbol{\tau}_{n,m} - \mathbf{T}|)}{|\boldsymbol{\tau}_{n,m} - \mathbf{T}|} + \frac{4\pi}{V_{\text{cell}}} \sum_{|\mathbf{G}| \neq 0} \frac{\cos(\mathbf{G} \cdot \boldsymbol{\tau}_{n,m})}{|\mathbf{G}|^2} e^{-|\mathbf{G}|^2 / 4\eta^2} \right] - \frac{1}{2} \left[\sum_{n} (Z_n^{\text{ion}})^2 \right] \frac{2\eta}{\sqrt{\pi}} - \frac{1}{2} \left[\sum_{n} Z_n^{\text{ion}} \right]^2 \frac{\pi}{\eta^2 V_{\text{cell}}}$$

where T and G are vectors of the real and reciprocal space lattices, respectively, and the real-space self-interaction terms $(\tau_{n,n})$ with T=0 are excluded. In this equation, η is a

parameter governing the separation of the electrostatic interactions into the short-range terms handled in real space (sum over T), and the long-range ones in reciprocal space (sum over G). Different choices of η can affect the speed of convergence of these sums but leave the final value for $E_{\rm Ewald}$ invariant.

This equation consists of sums and double sums over the atoms within the unit cell, which can be rewritten in terms of atomic contributions:

$$E_{\text{Ewald}} = \sum_{n} E_{\text{Ewald}}^{\text{atom } n} \tag{4}$$

witl

$$E_{\text{Ewald}}^{\text{atom}\,n} = Z_n^{\text{ion}} \left(\sum_m \frac{Z_m^{\text{ion}}}{2} \left[\sum_{\mathbf{T}} \frac{\text{erfc}(\eta | \boldsymbol{\tau}_{n,m} - \mathbf{T}|)}{|\boldsymbol{\tau}_{n,m} - \mathbf{T}|} + \frac{4\pi}{V_{\text{cell}}} \sum_{|\mathbf{G}| \neq 0} \frac{\cos(\mathbf{G} \cdot \boldsymbol{\tau}_{n,m})}{|\mathbf{G}|^2} e^{-|\mathbf{G}|^2/4\eta^2} \right] - \frac{\eta Z_n^{\text{ion}}}{\sqrt{\pi}} - \left(\sum_m Z_m^{\text{ion}} \right) \frac{\pi}{2\eta^2 V_{\text{cell}}} \right)$$
(5)

From this equation, we can begin to see the origins of the negative CP flooding over softer atoms. The contribution of each atom to the E_{Ewald} is proportional to the number of electrons (Z_n^{ion}) it contributes to the valence set. This can lead to very uneven contributions to the E_{Ewald} from the atoms of the system, particularly when valence-only and semicore pseudopotentials are mixed. For example, in CaAl₂ with valence-only pseudopotentials on both atoms, the Ewald contributions are -2.31 Ha from Al and -1.43 Ha from Ca. When a semicore pseudopotential is used for Ca, taking it from $Z^{\text{ion}} = 2$ to $Z^{\text{ion}} = 10$, the Ewald contribution from Ca is raised to -21.55 Ha (with the Al component now being -3.61 Ha). This results in a much more negative E_{Ewald} for the system, which is balanced around the Ca atoms by the large positive pressures decorating the core regions but washes out any positive core response from the Al atoms, biasing their interactions toward negative CPs.

What might be a better way of mapping the $E_{\rm Ewald}$? One simple approach is to consider whether every electron that an atom contributes to the system should also be contributing to the homogeneous background pressure. For example, semicore electrons could be considered to be so localized to their ion core that their contribution to the Ewald energy should be mapped locally to that atom rather than distributed over the whole structure.

Formally, this can be done by splitting the $Z_n^{\rm ion}$ variables into two terms: $Z_n^{\rm ion} = Z_n^{\rm itin} + Z_n^{\rm loc}$, corresponding to the numbers of electrons each atom contributes that should be considered as itinerant over the structure (from the point of view of the $E_{\rm Ewald}$, rather than in the sense of metallic conductivity) and localized to their atom of origin, respectively. Upon making this substitution in eq 4, the Ewald energy can be separated into a term that depends exclusively on the $Z_n^{\rm itin}$ values and one that includes the effects of the localized electrons:

$$E_{\rm Ewald} = E_{\rm Ewald}^{\rm itin} + E_{\rm Ewald}^{\rm loc} \tag{6}$$

where

The Journal of Physical Chemistry A

$$E_{\text{Ewald}}^{\text{itin}} = \sum_{n,m} \frac{Z_n^{\text{itin}} Z_m^{\text{itin}}}{2} \left[\sum_{\mathbf{T}} \left(\frac{\text{erfc}(\eta | \boldsymbol{\tau}_{n,m} - \mathbf{T}|)}{|\boldsymbol{\tau}_{n,m} - \mathbf{T}|} + \frac{4\pi}{V_{\text{cell}}} \sum_{\mathbf{G} \neq 0} \frac{\cos(\mathbf{G} \cdot \boldsymbol{\tau}_{n,m})}{|\mathbf{G}|^2} e^{-|\mathbf{G}|^2/4\eta^2} \right) - \frac{\pi}{\eta^2 V_{\text{cell}}} \right]$$

$$- \sum_{n} \frac{Z_n^{\text{itin}} Z_n^{\text{itin}}}{2} \frac{2\eta}{\sqrt{\pi}}$$
(7)

corresponds simply to the Ewald energy for a system with the ion cores having charges of Z_n^{itin} . The remainder has a more

$$E_{\text{Ewald}}^{\text{loc}} = \sum_{n} Z_{n}^{\text{loc}} \left\{ \sum_{m} \left(Z_{m}^{\text{itin}} + \frac{1}{2} Z_{m}^{\text{loc}} \right) \right.$$

$$\times \left[\sum_{\mathbf{T}} \frac{\text{erfc}(\eta | \mathbf{\tau}_{n,m} - \mathbf{T}|)}{|\mathbf{\tau}_{n,m} - \mathbf{T}|} \right.$$

$$+ \frac{4\pi}{V_{\text{cell}}} \sum_{\mathbf{G} \neq 0} \frac{\cos(\mathbf{G} \cdot \mathbf{\tau}_{n,m})}{|\mathbf{G}|^{2}} e^{-|\mathbf{G}|^{2}/4\eta^{2}} - \frac{\pi}{\eta^{2} V_{\text{cell}}} \right]$$

$$- \left(Z_{n}^{\text{itin}} + \frac{1}{2} Z_{n}^{\text{loc}} \right) \frac{2\eta}{\sqrt{\pi}} \right\}$$
(8)

But, as is evident from its form as a sum over ions n, this expression can still be partitioned into contributions from individual atoms.

Once this breakdown of the $E_{\rm Ewald}$ is made, a path opens to reducing the negative background pressure to accommodate softer atomic pseudopotentials. Consider again the case of CaAl₂ modeled with a semicore Ca pseudopotential, in which the Ca 3s²3p⁶ electrons are considered part of the valence set. If we assign each Ca atom's eight semicore electrons as localized, the Ca localized Ewald component comes to -22.85Ha out of the total -24.25 Ha for the Ca atom, which is nearly an order of magnitude larger that the Al atoms' Ewald contributions of -2.26 Ha/atom. If we were to remove this localized Ewald component from the homogeneous background (concentrating it instead around the Ca atoms), each Ca then adds only -1.40 Ha to the homogeneous part. This redistribution would greatly reduce the negative CP background, allowing a greater positive core response on the Al atoms to emerge.

In implementing such a scheme, we face the issue of how the localized atomic Ewald energies should be distributed around their respective atoms. To explore this question, we have tested a number of schemes. We first tried a homogeneous distribution of the energies within atomic cells defined for each atom as the volume where it has the largest weight in the Hirshfeld scheme. However, this results in discontinuous steps in the CP map at the atomic cell boundaries and relatively poor agreement between CP schemes calculated using semicore and valence-only pseudopotentials of the same element (see the Supporting Information).

We then considered mappings of the localized Ewald energies which would generate a more continuous CP map. Such functions would have a large proportion of the localized Ewald energies near the atom cores and near negligible amounts at larger distances from the atomic center. On this

basis, we tested schemes in which an atom's localized Ewald energy is distributed to the voxels within its atomic cell in proportion to either the semicore electron density at that voxel or the total DFT electron density at that voxel. As is demonstrated in the Supporting Information, the use of the total electron density as a weighting function gives CP schemes with greater consistency between pseudopotential choices than using the semicore density. The success of this approach may stem from its tendency to spread the localized Ewald energy over a radial extent similar to that of the atom's positive CP core features.

In Figure 5, we illustrate the effect that such a reallocation of the localized Ewald energies on the Ca has on the overall CP map of CaAl₂ calculated with a semicore Ca pseudopotential. In the original CP map (Figure 5a), the Al atoms are again nigh indistinguishable from the negative background pressure. A CP = 0.0 contour is drawn over the map in black, from

CP maps with Semicore Ca pseudopotential

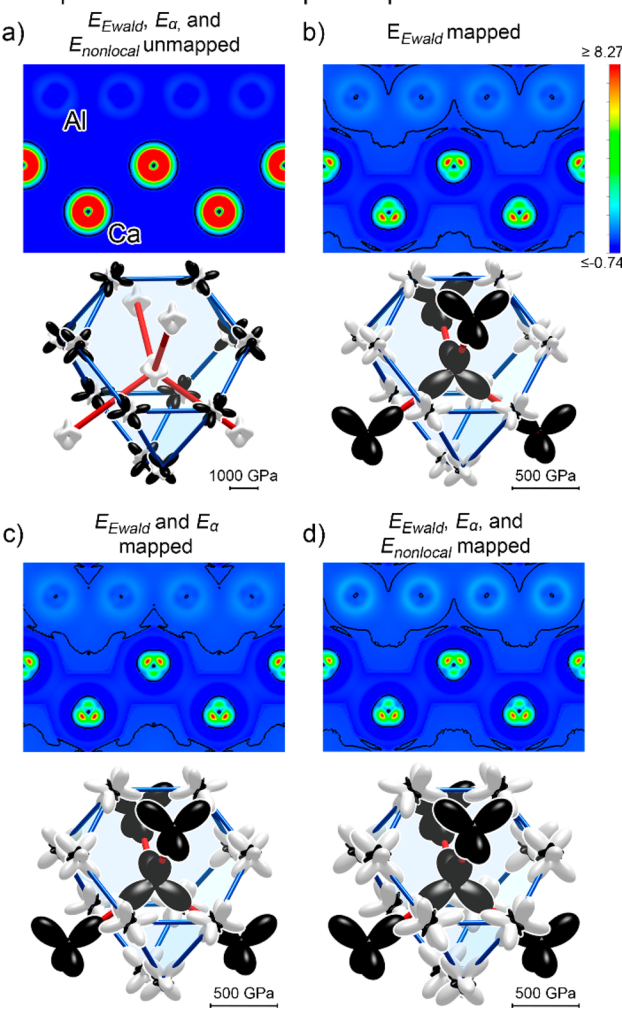


Figure 5. Revised mapping of terms previously homogeneously distributed in the CP analysis of CaAl₂ (calculated with a Ca semicore pseudopotential). The CP cross-section and integrated scheme obtained with the original CP method are first shown in (a), with the revised mapping of the (b) semicore Ewald, (c) E_{α} , and (d) nonlocal pseudopotential energies being turned on in sequence. Integrated CP schemes (generated assuming atomic charges equal to 50% of those obtained from a Bader analysis, i.e., 50% ionicity) are shown.

which it can be seen that the CP in the Al regions is entirely negative. After the localized Ewald contributions were reallocated to the Ca atoms (Figure 5b), the map changes dramatically. Through the reduction in the negative background pressure, relatively large volumes surrounding the Al atoms now have positive values of CP. The Ca core regions also are starkly different, with much more anisotropic features than before.

This mapping also has consequences for the integrated CP scheme, as shown with 50% ionicity in the lower panels of the figure. Without the Ewald redistribution the scheme shows negative pressures along the Al–Al contacts and positive pressures along the Ca–Al ones, in opposition to the expectations derived from the phonon band structure and the CP results of the isostructural CaPd₂ phase. After the Ewald redistribution is turned on, the decreased negative pressure background in the Al region allows positive Al–Al CPs to emerge, with the Ca–Al CPs now being negative. The Al CP quadrupole implied by the phonon frequencies is now achievable, illustrating the benefits of treating semicore electrons as localized in the mapping of the $E_{\rm Ewald}$.

3.3.2. E_{α} Term. The Ewald energy involves a homogeneous electron gas interacting with point charges placed at the ion core positions. Of course, the ion cores are not simply point charges but have a more complex local potential reflecting the presence of the core electrons. This correction factor owing to the difference between the potentials used in $E_{\rm Ewald}$ and in the ion cores of the true system is the E_{α} component of the total energy, written as 62

$$E_{\alpha} = \left(\sum_{n} \alpha_{n}\right) \frac{N_{\text{electrons}}}{V_{\text{cell}}} \tag{9}$$

where α_n is just the integrated difference between the local pseudopotential for atom n and the potential for a point charge:

$$\alpha_n = \int 4\pi r^2 \, \mathrm{d}r \left[V_{\text{local}}^n(r) - \left(-\frac{Z_n^{\text{ion}}}{r} \right) \right] \tag{10}$$

Following our treatment of E_{Ewald} , E_{α} can be similarly divided into itinerant and localized terms:

$$E_{\alpha} = \frac{N_{\text{electrons}}}{V_{\text{cell}}} \sum_{n} \alpha_{n} = \frac{\left(\sum_{n'} Z_{n'}^{\text{ion}}\right)}{V_{\text{cell}}} \sum_{n} \alpha_{n}$$

$$= \left(\sum_{n'} Z_{n'}^{\text{ion}}\right) \sum_{n} \frac{\alpha_{n}}{V_{\text{cell}}} = \left(\sum_{n'} Z_{n'}^{\text{loc}}\right) \sum_{n} \frac{\alpha_{n}}{V_{\text{cell}}}$$

$$+ \left(\sum_{n'} Z_{n'}^{\text{itin}}\right) \sum_{n} \frac{\alpha_{n}}{V_{\text{cell}}}$$

$$= E_{\alpha}^{\text{loc}} + E_{\alpha}^{\text{itin}}$$
(11)

With this partitioning, the localized atomic E_{α} contributions can be calculated and mapped to atomic regions alongside their $E_{\rm Ewald}$ counterparts. However, as is shown in Figure 5c for CaAl₂, the pressures arising from E_{α} are small enough that such a spatial resolution has little consequence for a compound's CP scheme.

3.3.3. Nonlocal Pseudopotential Contributions. The nonlocal pseudopotential energy arises from differential screening of the s-, p-, d-, and f-components of the pseudo-

wavefunctions. The analytical form of the Hartiwigsen–Goedecker–Hutter (HGH) norm-conserving pseudopotentials ⁵⁰ used in this work makes it possible to construct maps of these contributions using the planewave coefficients from the one-electron pseudo-wavefunctions. For each atomic pseudopotential, the nonlocal contributions are given by separable operators of the form:

$$\hat{V}_{\text{nonlocal}}^{n} = \sum_{l=0}^{3} \sum_{m=-l}^{l} \sum_{i=1}^{3} \sum_{j=1}^{3} |P_{lm,i}^{n}\rangle h_{l,ij}^{n} \langle P_{lm,j}^{n}|$$
(12)

with

$$\langle P_{lm,j}^n | \psi \rangle = \iiint p_{l,j}^n(\mathbf{r}) Y_{lm}^*(\hat{\mathbf{r}}) \psi(\mathbf{r}) d\mathbf{r}$$
 (13)

where the $p_{l,j}^n(r)$'s are Gaussian functions tightly focused around the atomic center defined by parameters in the pseudopotential, and a local coordinate system is used in which r = 0 at the nucleus.

In this way, the Kohn–Sham Hamiltonian matrix element between a pair of basis functions gains contributions of the $h^n_{l,ij}$ terms weighted by the degree to which the functions share s-, p-, d-, and f-character in the core regions for l=0,1,2, and 3, respectively, with the different Gaussians indexed by i and j allowing for different radial extents to be explored. In particular, the matrix elements between two planewaves are given by

$$V_{\text{nonlocal},\mathbf{k}\mathbf{k}'}^{n} = \sum_{l=0}^{3} \sum_{m=-l}^{l} \sum_{i=1}^{3} \sum_{j=1}^{3} \langle \mathbf{k} | P_{lm,i}^{n} \rangle h_{l,ij}^{n} \langle P_{lm,j}^{n} | \mathbf{k}' \rangle$$

$$= \sum_{l=0}^{3} \sum_{m=-l}^{l} \sum_{i,j=1}^{3} Y_{lm}(\hat{\mathbf{k}}) p_{l,i}^{n}(k) h_{l,ij}^{n} p_{l,j}^{n}(k') Y_{lm}^{*}(\hat{\mathbf{k}}')$$
(14)

where the functional forms of the $p_{l,j}^n(k')$ functions are provided in the original HGH paper.⁵⁰

With this equation for the nonlocal planewave matrix elements, contributions to the nonlocal energy can be resolved by atom and *l*-component:

$$E_{\text{nonlocal}} = \sum_{n} \sum_{l=0}^{3} E_{\text{nonlocal},l}^{n}$$
(15)

Once these terms are obtained, we are now faced with the issue of how they should be mapped spatially around their corresponding atoms. While numerous choices are available, the differential screening of the different l-components is an effect associated with the core of the atom, where the potential is expected to be largely spherically symmetric. The major challenge is then to decide how tightly these terms should be localized to the core of the atom. The form of the nonlocal operators in eq 12 provides some guidance here. The nonlocal energy component from eigenstate ψ_{ν} contains terms of the form

$$\iiint d\mathbf{r} d\mathbf{r}' Y_{lm}(\hat{\mathbf{r}}) Y_{lm}^*(\hat{\mathbf{r}}') h_{l,ij}^n p_{l,i}^n(r) p_{l,j}^n(r') \psi_{\nu}^*(\mathbf{r}) \psi_{\nu}(\mathbf{r}')$$
(16)

whose r=r' components are simply the electron density contribution from that state weighted by a product of two core-centered Gaussian functions and an angular function. The contributions from different r values will then be strongest where the $p_{l,i}^n(r) p_{l,j}^n(r)$ and $\psi_{\nu}^*(\mathbf{r}) \psi_{\nu}(\mathbf{r})$ products are simultaneously large. Distributions of the $E_{\mathrm{nonlocal},l}^n$ terms that behave

in this way can be constructed by replacing the Y_{lm} terms with 1 to produce a spherically symmetric projector and the wavefunction terms $\psi_{\nu}^*(\mathbf{r}) \psi_{\nu}(\mathbf{r}')$ with the electron density $\rho(\mathbf{r})$, while setting $\mathbf{r} = \mathbf{r}'$:

$$E_{\text{nonlocal},l}^{n}(\mathbf{r}) = \frac{E_{\text{nonlocal},l}^{n}}{N} \sum_{i,j=1}^{3} h_{l,ij}^{n} p_{l,i}^{n}(|\mathbf{r} - \mathbf{r}_{n}|) p_{l,j}^{n}(|\mathbf{r} - \mathbf{r}_{n}|) \rho(\mathbf{r})$$
(17)

where

$$N = \iiint \sum_{i,j=1}^{3} h_{l,ij}^{n} p_{l,i}^{n} (|\mathbf{r} - \mathbf{r}_{n}|) p_{l,j}^{n} (|\mathbf{r} - \mathbf{r}_{n}|) \rho(\mathbf{r}) d\mathbf{r}$$
(18)

with \mathbf{r}_n being the position of atom n.

How does this mapping of the nonlocal energies affect the CP scheme of CaAl₂? In Figure 5, we continue with the case of Ca being treated with a semicore pseudopotential. The atomic nonlocal pressures of the Al atoms are positive (5.5 GPa/atom) and yield positive CP contributions, while those of the Ca are negative (-23.9 GPa/atom). The mapping of these positive nonlocal pressures near the Al atomic centers then leads to a small enhancement of their core responses. The CP features near the Ca atoms, meanwhile, are lessened, permitting anisotropic core features to surface. In the integrated scheme, this results in even stronger positive Al—Al CPs and more significant Al CP quadrupoles.

The importance of the nonlocal CP contributions is more pronounced in the case where Ca is modeled with a valence-only pseudopotential, and thus no localization of the $E_{\rm Ewald}$ or E_{α} terms is applicable. In the original scheme, the CP features on the Al atoms are reversed relative to the dictates of the phonon band structure (Figure 6a), just as in the semicore case. Turning on the mapping of the Al nonlocal pressures leads to much more significant positive core responses around the Al atoms. The nonlocal atomic pressures for the Ca,

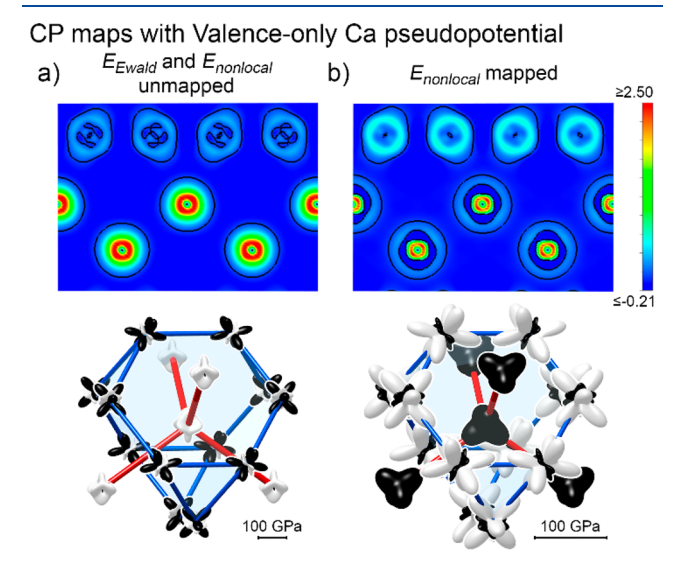


Figure 6. CP maps and integrated schemes for CaAl₂ calculated with a valence-only pseudopotential for the Ca atoms. (a) With homogeneous mapping of the Ewald and nonlocal components, only a minimal core response on the Al atoms is achievable. (b) With mapping of the nonlocal energy, stronger positive Al core responses appear. The integrated CP schemes were generated by assuming atomic charges equal to 50% of those obtained from a Bader analysis.

however, are negative, and mapping them leads to a reduction of the positive core responses on the Ca. The combined effect is that the integrated CP scheme (Figure 6b) now shows positive Al–Al CPs and negative Ca–Al ones, in agreement with our analysis of the frequencies of the structure's phonon modes. The final scheme also shows close correspondence to that obtained with a Ca semicore pseudopotential once the localized $E_{\rm Ewald}$, E_{ar} and $E_{\rm nonlocal}$ terms are mapped (Figure 5d).

The integrated schemes shown so far have been generated by assuming that the charges on the Ca and Al are 50% of those obtained in a Bader charge analysis. We are now in a position where we can fine-tune the CP scheme through adjustments of the atomic charges used in the Hirshfeld-inspired scheme for constructing contact volumes. In the case of CaAl₂, with Bader charges of +1.2 on Ca and -0.6 on Al, the large occupancy of the 3p orbital for an Al^{0.6-} anion prevented us from being able to obtain a converged ground state far beyond 75% of this charge. Nonetheless, the 0% to 75% ionicity range of charges is sufficient to see the role that this parameter plays in the analysis.

For the results of both pseudopotentials with neutral free atomic electron densities, the Al–Al contacts (as well as the Ca–Ca ones for the valence-only Ca case) display positive CPs while the Ca–Al contacts show negative CP (Figure 7, top). At higher ionicities, these Al–Al positive CPs persist, as could be expected from the growing size of the Al anions. The Ca–Al contacts remain characterized by negative CP as well. The only major change across the schemes is the growth of negative CP along the Ca–Ca contacts with increasing ionicity, reflecting the decrease in the effective size of the Ca cations.

The classic sphere packing model of the MgCu₂ type, as analyzed with near-neighbor diagrams by Pearson,⁶ provides a useful framework for interpreting these trends. If we consider an AB₂ MgCu₂-type Laves phase as a packing of hard spheres with radii r_A and r_B , it is impossible to achieve contacts between the A and B spheres without forcing overlap at the A–A or B–B contacts. At the ideal radius radio r_A/r_B = 1.225, the B spheres and A spheres are in contact with each other along the homoatomic contacts, leaving gaps along the A-B interatomic paths. Obtaining shorter A-B distances would then require the spheres to overlap or flatten at the A–A and B-B contacts, a conflict that corresponds well to the 0% ionicity, valence-only Ca CP scheme in Figure 7, where Ca-Al negative CPs are countered by positive Al-Al and Ca-Ca CPs. For smaller r_A/r_B ratios, the gaps appear along both the A-A and A-B interatomic paths, which are now prevented from closing solely by the B-B contacts. This picture coincides with the CP schemes with increased ionicity, where both the Ca-Al and Ca-Ca interactions are marked by negative CP and resisted only by the Al-Al interactions.

The Al CP quadrupoles that appear across these schemes are in close accord with our analysis of the phonon modes of the system. For a range of ionicity choices, vibrations corresponding to contractions of the Al tetrahedra are now correctly predicted to be stiff by the CP schemes, with softer modes being expected for the twisting of the Al tetrahedra.

As we described in section 3.2, it is more difficult to derive a clear prediction for the sign of the Ca—Ca pressure from the phonon frequencies. We can note, though, that the placement of the mode with out-of-phase motions at the bottom of the phonon band structure would point toward the negative Ca—Ca CPs seen at higher ionicities. These schemes at ionicities between 50 and 75% have the added advantages of showing

The Journal of Physical Chemistry A

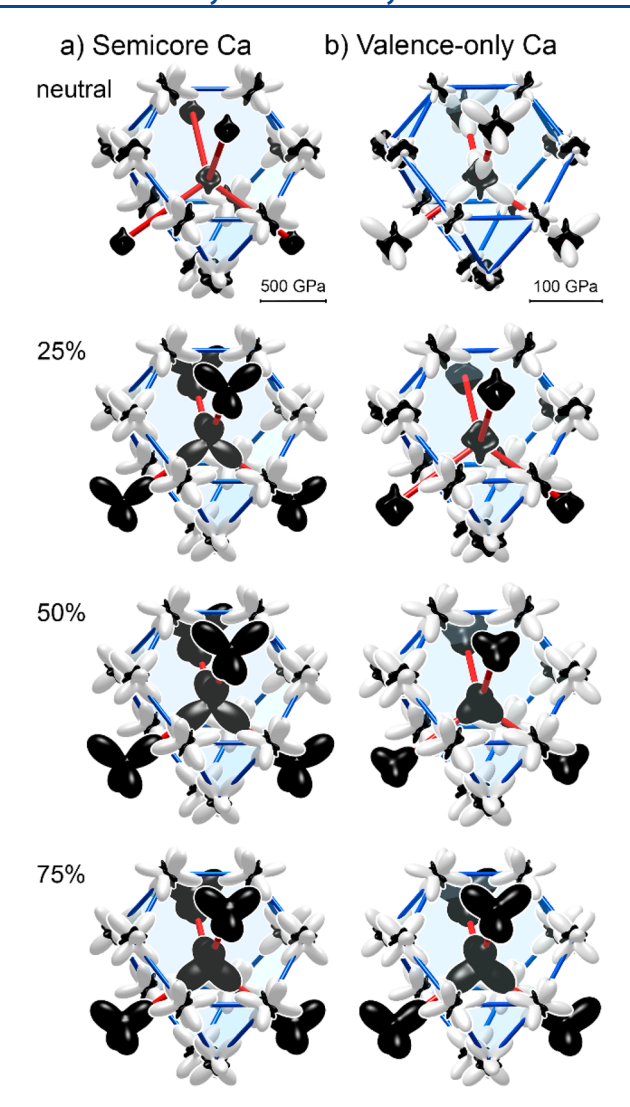


Figure 7. CP schemes of CaAl₂ with (a) semicore and (b) valenceonly pseudopotentials on Ca. Nonlocal energies are mapped, as well as the localized Ewald energy and E_{α} for CaAl₂ with a semicore Ca pseudopotential. As the ionicity is raised, the Ca–Ca CPs become increasingly negative, reflecting the smaller size of the Ca cation. The Al–Al CPs are positive throughout.

qualitative agreement between the schemes calculated with semicore and valence-only pseudopotentials, and involving atomic charges similar to those expected for the system.

Overall, then, the revised mapping of the localized $E_{\rm Ewald}$, E_{ω} and $E_{\rm nonlocal}$ terms have addressed the challenges we originally encountered for CaAl₂.

Upon applying the revised method to the CP analysis of CaPd₂, we obtain a picture similar to that of CaAl₂ (see the Supporting Information for a range of pseudopotential choices). The presence of CP quadrupoles on the Pd atoms persists across these schemes for reasonable choices of the ionicity. The Ca—Ca contacts, however, are now marked by negative CP, without the positive lobes that we earlier used to explain the relative ordering of the phase's Ca-based phonon modes. In section 3, though, we saw that such positive Ca—Ca CPs are not essential to interpretating the features of the phonon band structure: the involvement of the heavier Pd atoms in the in-phase mode but not the out-of-phase mode can also explain their order in frequency.

3.4. Demonstration: Origins of the La₃Al₁₁ Type. New opportunities emerge from the revisions to the CP approach described in the previous sections: intermetallic aluminides exhibit a diverse structural chemistry that ranges from simple variants of the fcc and bcc structures to icosahedral and decagonal quasicrystals, 70-73 but the softness of the Al pseudopotentials has limited the insights obtainable with the CP method for these systems. To illustrate these new opportunities, let us consider a moderately complex structure, La₃Al₁₁. ⁴⁵ This compound represents a vast family of structures that can be derived from the simple BaAl4 type, including the CaAl₄ and EuIn₄ types^{74,75} as well as the structures of La₂NiAl₇⁷⁶ and RE₇Zn₂₁Tt₂. The La₃Al₁₁ type itself is also parent to a number of ternary variants, including ${\rm Tb_3Zn_{3.6}Al_{7.4}}^{78}$ Dy₃Co₆Sn₅, 79 Eu₃Ag₂In₉, 80 and Y₃Cu₄Ga₇, with varying degrees of order in their coloring patterns. The electronic driving forces stabilizing the La₃Al₁₁ type and its parent structure have been explored extensively with theoretical calculations, but the role of atomic size has been so far inferred largely from indirect or empirical considerations. 14,39,82

We begin by showing how the La₃Al₁₁ structure is derived from the BaAl₄ type (Figure 8). In the BaAl₄ type, square nets

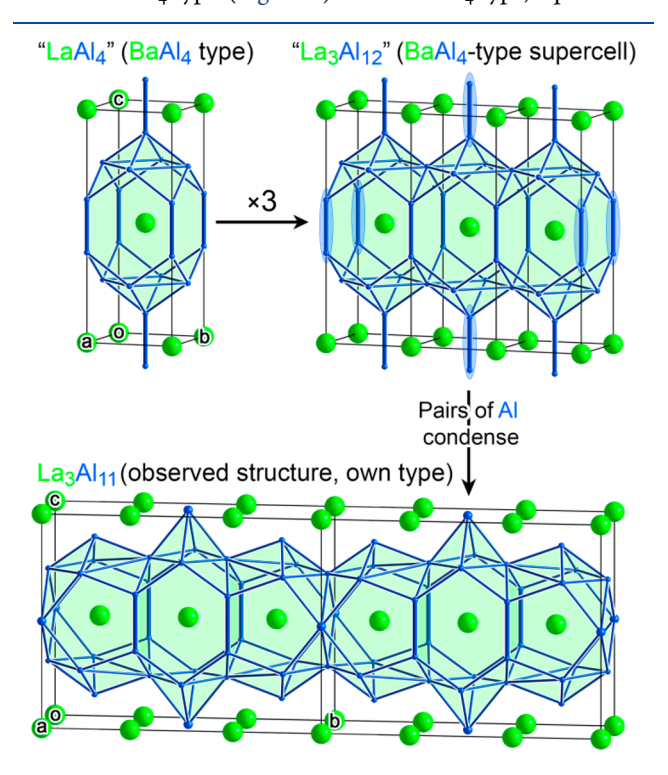


Figure 8. The structure of La_3Al_{11} derived from a hypothetical $BaAl_4$ -type parent compound. To aid visualization, sets of space-filling volumes centered by the La atoms are highlighted in light green.

of Al are capped above and below on alternate squares to make sheets (which, in fact, are layers of edge-sharing $Al@Al_4$ tetrahedra). These layers stack up along c such that each of the outer atoms finds a neighbor directly above or below in the next layer. This creates 16-coordinate polyhedra that accommodate the cations (shown in Figure 8 with two additional capping atoms to create space-filling volumes, for ease of visualization). To see the relationship of this structure to that of La_3Al_{11} , we first move to a $3 \times 1 \times 1$ supercell of "LaAl4", producing a structure with a formula unit of "La3Al12".

The La₃Al₁₁ composition is then obtained by condensing a selection of the Al₂ pairs into single Al atoms where the Al layers meet (one Al₂ pair per formula unit, or two per cell where Z=2). The full La₃Al₁₁ structure is then obtained as the structure relaxes around the substituted atoms, with 2/3 of the La cations now having coordination numbers of 14 instead of 16, and appearing to lie in pseudopentagonal channels along the a axis rather than hexagonal ones.

Such a contraction of the cation coordination environments upon replacing Ba with La would seem to be in agreement with the expectations of atomic size, with the metallic radius of La being significantly smaller than that of Ba (1.87 Å vs 2.22 Å). Using CP analysis, we can now test this notion and explore the details of the driving forces leading to the $\text{La}_3\text{Al}_{11}$ structure.

We begin by exploring the CP tensions present in a hypothetical BaAl₄-type LaAl₄ structure that might anticipate the formation of the more complex observed structure. In Figure 9a, we show CP schemes calculated for this LaAl₄ structure using (1) the original homogeneous mapping of the $E_{\rm Ewald}+E_{\alpha}+E_{\rm nonlocal}$ terms and (2) the full mapping of the $E_{\rm nonlocal}$ term and the localization of the $E_{\rm Ewald}+E_{\alpha}$ contributions from the La semicore electrons to the La atomic regions. The charges for both schemes are set to 75% of the Bader charges. In the Supporting Information, versions calculated with varying ionicity values are also provided, illustrating that this parameter has little influence on the overall CP features.

As in our earlier analysis of CaAl₂, the revised mapping of the $E_{\rm Ewald}+E_{\alpha}+E_{\rm nonlocal}$ terms leads to drastic effects on the CP scheme of LaAl₄. With homogeneous mapping of these contributions, the interactions involving La atoms mostly show positive pressures, in line with the strong core responses expected from the La semicore electrons. Meanwhile, the Al–Al interactions are marked with negative pressure, as is predestined by their small core responses and the depth of the negative pressure background arising from the total Ewald energy. Applying the new mapping (Figure 9a, right) essentially reverses the picture: the Al–Al short contacts now have primarily positive CP, while the La–Al contacts are decorated by negative CP.

Which of these CP schemes provides a better description of the interactions within this structure? To answer this question, we turn to the phonon band structure of LaAl₄ calculated after a full structural relaxation (Figure 9b), focusing on a selection of the modes at Γ as shown in Figure 9c. Upon overlaying the phonon modes with the CP lobes calculated with the revised mapping, simple interpretations of their relative frequencies begin to take shape. In the lower frequency modes (Figure 9c, bottom), the arrows corresponding to atomic motions tend to lengthen or at least leave fixed contacts with positive CP, or else run along directions of negative CP. For example, in the lowest frequency mode, zigzag chains of Al atoms defined by positive CPs move past each other as rigid units, which serve to lengthen the Al-Al contacts with positive CP between the rigid chains. In the next mode (frequency = 3.60 THz), the Al-Al distances are held essentially constant as the Al and La sublattices move against each other along the negative La-Al CPs.

This is in contrast to the picture painted by the high frequency modes (Figure 9c, top). In one of these modes (frequency = 9.48 THz), the Al–Al distances within the layers of Al tetrahedra (positive CP) oscillate, with little net change to the average La–Al distances. The highest frequency mode at

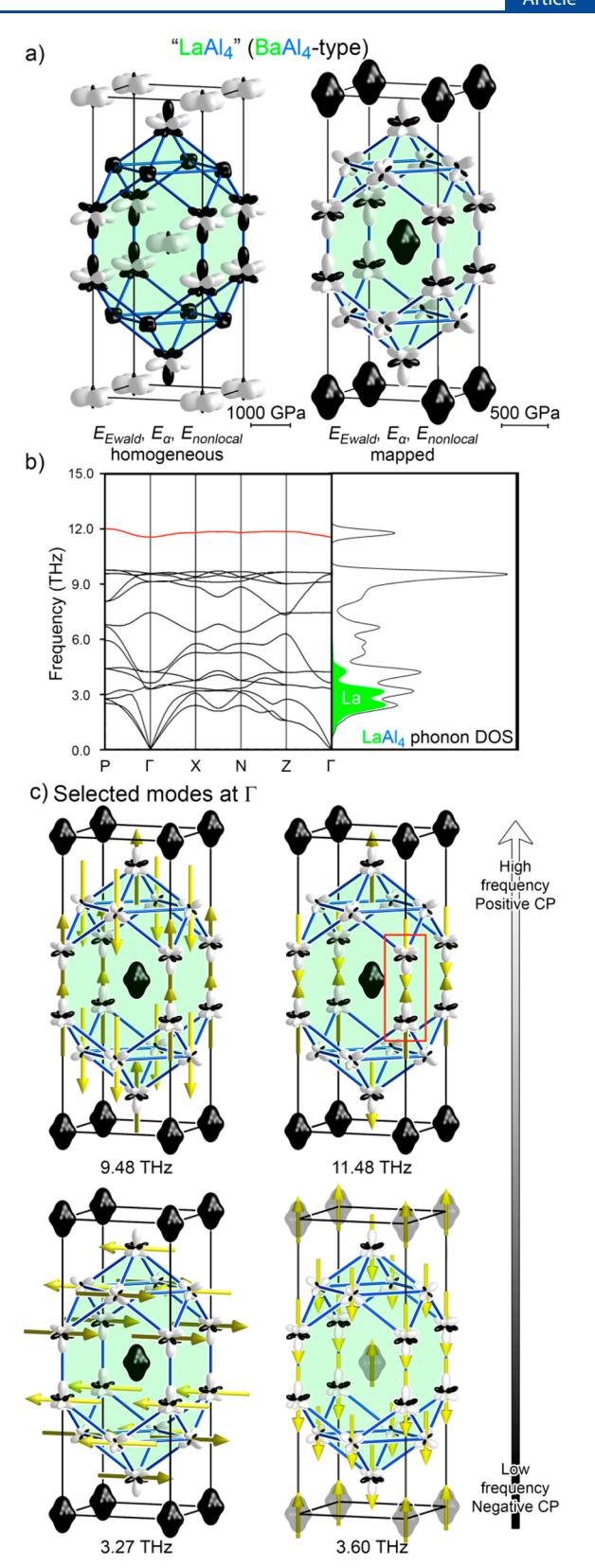


Figure 9. Correspondences between the CP schemes and the phonon band structure of a hypothetical BaAl₄-type LaAl₄ phase. (a) CP schemes calculated with the original and revised mappings of the $E_{\rm Ewald}$, E_{ω} and $E_{\rm nonlocal}$ terms. (b) Phonon band structure and DOS distribution, with the contributions from the La atoms shaded. (c) Selected modes at the Γ point overlaid with the CP scheme obtained with the revised method.

 Γ forms part of a narrow band that stretches across the band structure diagram (Figure 9b, highlighted in red); it involves the stretching and contraction of the interlayer Al pairs, where the strongest positive CPs are present in the structure. With the revised mapping, the CP scheme thus provides a simple guide to the relative phonon frequencies. The homogeneous mapping yields essentially the inverse scheme, and is thus clearly not consistent with the phonon band structure.

Now that we have validated the CP scheme derived from the revised $E_{\rm Ewald} + E_{\alpha} + E_{\rm nonlocal}$ mapping, what can we glean from it in terms of expectations for structural chemistry? The La atoms are dominated by negative CP, indicating that they are too small for their 16-coordinate polyhedra and are calling for the contraction of the structure. Meanwhile, the positive CPs between the Al atoms reveal the reason this structural contraction cannot occur: the Al atoms are already too tightly packed. The especially large positive CPs along the interlayer Al neighbors reveal the interlayer regions to be particularly strained parts of the Al lattice. These are the very Al pairs that undergo partial substitution by single atoms in the observed structure of $\rm La_3Al_{11}$. The hypothesis that size effects provide a driving force for the formation of this superstructure appears to be borne out by the CP scheme of its parent structure.

The ways in which the superstructure provides strain relief can be seen in the CP scheme of La₃Al₁₁ (Figure 10). The La atoms still experience negative CP, which again are balanced by positive CPs between the Al atoms. Overall, however, the magnitudes of the pressure features are lower than in the

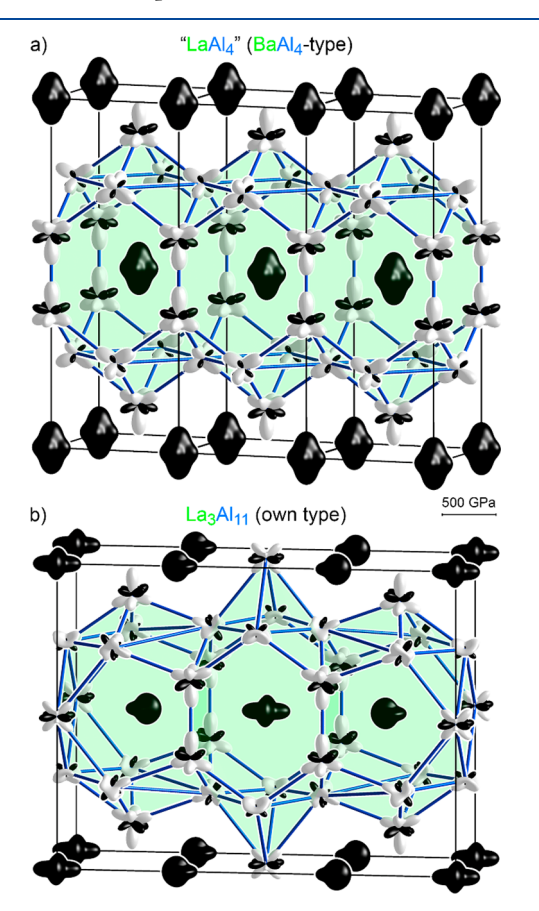


Figure 10. CP schemes illustrating relief on going from (a) a hypothetical BaAl₄-type LaAl₄ phase to (b) the observed structure of La₃Al₁₁.

original LaAl $_4$ scheme. This reduction can be rationalized from the Al $_2$ /Al substitution: the newly inserted Al atoms show much smaller CP lobes, both positive and negative, than the dumbbell atoms that they are replacing. They partake in longer Al–Al contacts and shorter La–Al ones than either of the Al atoms they replace. The surrounding Al atoms also achieve substantial CP relief, not only through longer distances to the newly substituted atoms but also through motions into the space formerly filled by the Al $_2$ dumbbells that alleviate strong positive CPs experienced by Al–Al contacts further away from the substitution sites. The Al $_2$ /Al substitution and the accompanying relaxation allow the Al sublattice to form a tighter grip on the La coordination environments, leading to less negative La–Al CPs.

The strongest residual positive CP features in the structure are on the remaining interlayer Al_2 dumbbells. One could then imagine continuing this process of decompressing the Al sublattice through Al_2/Al substitutions on the remaining sites. The end result would be a body-centered tetragonal lattice of cations, each with cuboctahedral coordination by Al atoms: the $TiAl_3$ structure type. The placement of $TiAl_3$ as the endmember in a CP-driven Al_2/Al substitution starting from the $BaAl_4$ type would be consistent with the trends in metallic radii on going from Ba to La to Ti.

4. CONCLUSIONS

In principle, the DFT-chemical pressure method offers a framework for giving precision to arguments based on atomic size effects across the chemistry of solid state materials. Over the course of this Article, we have worked toward the realization of this general applicability by delving into one of the most challenging cases for this method: systems including atoms whose pseudopotential's local components are so soft they appear to be largely unresponsive to compression by their neighbors. Through a comparison of the CP schemes and phonon band structures of CaPd2 and CaAl2, we illustrated how the atomic pseudopotential we use for Al can create just this scenario, with negative CPs persistently being found along the Al-Al contacts in sharp contrast to the stiffness of the Al-Al interactions evident in the phonon frequencies. These observations led us to reevaluate the components of the total energy which had previously been homogeneously mapped in the creation of the CP maps (the E_{Ewald} , E_{α} , and E_{nonlocal} energies) due to their lack of an unambiguous manner of decomposing them spatially. With a revised treatment of these terms, the responsiveness of the Al atoms to their surroundings became much more evident in their CP schemes. This allowed us to capture key aspects of the relative phonon frequencies in CaAl₂ and a hypothetical BaAl₄-type LaAl₄ structure, as well as to interpret the more complex La₃Al₁₁ structure as the result of a CP-driven Al₂ dumbbell/Al atom substitution from the BaAl₄

Through these analyses, we found that a correct mapping of the $E_{\rm Ewald}$ term, being one of the largest contributors to the total energy for densely packed arrays of metal atoms, can be among the most crucial to the CP map. Our approach to treating $E_{\rm Ewald}$ (along with E_{α}) here is to recognize that not all electrons in the valence set of a calculation are necessarily active in shaping the structure, but that some may be heavily localized to their parent atom. Mapping the energetic contributions from these localized electrons to their corresponding atoms could bring positive core responses from the remaining atoms to the foreground. A limitation of this

treatment, however, is the ambiguity we face in assigning the number of electrons on each atom that should be considered localized. In the current results and in our preliminary examination of a range of other systems, we have found that reasonable CP schemes can be fairly consistently obtained by simply equating the number of localized electrons contributed by an atom to the number of semicore electrons that atom contains. Care should be taken, though, to check the validity of this assignment for new systems, as can be done with comparisons of CP schemes calculated with different pseudopotential choices and calibrations against phonon band structure results.

The $E_{\rm nonlocal}$ term, meanwhile, is smaller than $E_{\rm Ewald}$ but can still play a large role in the core responses of soft pseudopotentials, as illustrated in the CP scheme of CaAl₂ modeled with a valence-only Ca pseudopotential. Unlike the case of $E_{\rm Ewald}$, partitioning of $E_{\rm nonlocal}$ into atomic contributions should likely be applied regardless of whether valence-only or semicore pseudopotentials are used.

Beyond the methodological developments, one theme to emerge from this work is the continued role of CP quadrupoles as strong indicators of soft atomic motions. In our previous analyses, the predictive nature of these features was apparent in transition metal-rich phases, as in the incommensurately modulated CaPd₅ phase³⁴ and the superconductor Nb₃Ge,³ where the majority atoms exhibited strong core responses. With the revisions to the CP method described here, these conclusions can be extended to systems, such as aluminides, where the core responses are more subtle. For both CaAl₂ and the hypothetical LaAl4 phase, the highest frequency phonon modes at the Γ point involved Al-Al contraction against the positive poles of their CP quadrupole, while those containing the perpendicular motions were among the softest of the optical modes. Together with the appearance of CP relief upon going from the hypothetical LaAl₄ structure to the observed La₃Al₁₁ superstructure, these results highlight how insights similar to those previously obtained for transition metal-based systems should now be available for aluminides and related phases. Along these lines, it will be interesting to explore how CP quadrupoles may underlie a broader range of structural phenomena in aluminides, such as disorder, modulations, and phase transitions.

In addition, the case of La₃Al₁₁ highlights how the substitution of atomic units can serve as a mechanism for CP relief, with a selection of particularly strained Al₂ dumbbells in the BaAl₄ type being replaced by single atoms. The Al₂/Al substitution is particularly suited to the specific geometrical situation as it replaces eight overly short Al–Al contacts with longer ones, while exchanging eight overly long Al–La contacts for four shorter ones. This is the reverse case of the Th₂Zn₁₇ structure type that we analyzed previously,³³ where single cations were partially replaced by transition metal dumbbells to achieve CP relief. One might wonder whether analogous CP features in other simple crystal structures may yield similar tendencies for atom/dumbbell interchange.

Finally, while our focus has been on intermetallic aluminides in this work, this choice was based on the particular challenges they pose for CP analysis. The improvements to the CP method presented here should enhance its abilities to elucidate the role atomic size plays in other inorganic materials. We are looking forward to exploring the degree to which the revised method can serve as a general tool for analyzing structural

chemistry in the solid state, and seeing where new limiting factors may arise.

ASSOCIATED CONTENT

S Supporting Information

The Supporting Information is available free of charge on the ACS Publications website at DOI: 10.1021/acs.jpca.8b07419.

Additional computational details, including k-point and energy cutoffs, DFT-optimized geometries, total energies, and fractional atomic coordinates; chemical pressure results for CaPd2 with varying pseudopotential and ionicity options; chemical pressure results for BaAl4-type LaAl4 calculated with a variety of mapping options and ionicities; chemical pressure schemes for La3Al11 calculated with a range of ionicities; phonon DOS distributions for CaPd2 and CaAl2 obtained with different pseudopotential options; images of the complete sets of Γ -point phonon modes for CaAl2 and BaAl4-type LaAl4; plots of the Bader charges from electron densities obtained from PAW-GGA and PAW-LDA calculations (PDF)

AUTHOR INFORMATION

Corresponding Author

*D. C. Fredrickson. E-mail: danny@chem.wisc.edu.

ORCID ®

Daniel C. Fredrickson: 0000-0002-3717-7008

Author Contributions

The manuscript was written through contributions of all authors. All authors have given approval to the final version of the manuscript.

Note:

The authors declare no competing financial interest.

ACKNOWLEDGMENTS

We thank Erdong Lu for helpful discussions regarding the methodology improvements described in this Article as well as for preliminary calculations on the CaAl₂ structure, and Dr. Vincent Yannello for CP calculations on the La₃Al₁₁ structure using the original methodology. We are also grateful to Hillary Mitchell Warden, Gordon Peterson, Kendall Kamp, and SangWon Park for sharing their experiences with the revised CP methods as they applied them to their own systems. We gratefully acknowledge the financial support of the National Science Foundation through grants DMR-1508496 and DMR-1809594. This work made use of computational resources supported by NSF grant CHE-0840494.

REFERENCES

- (1) Müller, U. Inorganic Structural Chemistry; Wiley: Chichester, U.K., 1993.
- (2) Waber, J. T.; Cromer, D. T. Orbital Radii of Atoms and Ions. *J. Chem. Phys.* **1965**, *42*, 4116–4123.
- (3) Kammeyer, C. W.; Whitman, D. R. Quantum Mechanical Calculation of Molecular Radii. I. Hydrides of Elements of Periodic Groups IV through VII. *J. Chem. Phys.* **1972**, *56*, 4419–4421.
- (4) Zunger, A. Systematization of the Stable Crystal Structure of All AB-Type Binary Compounds: A Pseudopotential Orbital-Radii Approach. *Phys. Rev. B: Condens. Matter Mater. Phys.* **1980**, 22, 5839–5872.
- (5) Bader, R. F. W. Atoms in Molecules: A Quantum Theory; Clarendon Press: Oxford, U.K., 1994.

- (6) Baranov, A.; Kohout, M.; Wagner, F. R.; Grin, Y.; Kniep, R.; Bronger, W. On the Volume Chemistry of Solid Compounds: the Legacy of Wilhelm Biltz. *Z. Anorg. Allg. Chem.* **2008**, 634, 2747–2753.
- (7) Bultinck, P.; Van Alsenoy, C.; Ayers, P. W.; Carbó-Dorca, R. Critical Analysis and Extension of the Hirshfeld Atoms in Molecules. *J. Chem. Phys.* **2007**, *126*, 144111.
- (8) Bultinck, P.; Ayers, P. W.; Fias, S.; Tiels, K.; Van Alsenoy, C. Uniqueness and Basis Set Dependence of Iterative Hirshfeld Charges. *Chem. Phys. Lett.* **2007**, 444, 205–208.
- (9) Vanpoucke, D. E. P.; Bultinck, P.; Van Driessche, I. Extending Hirshfeld-I to Bulk and Periodic Materials. *J. Comput. Chem.* **2013**, *34*, 405–417.
- (10) Lillestolen, T. C.; Wheatley, R. J. Atomic Charge Densities Generated Using an Iterative Stockholder Procedure. *J. Chem. Phys.* **2009**, *131*, 144101.
- (11) Hume-Rothery, W.; Raynor, G. V. The Structure of Metals and Alloys, 4th ed.; Institute of Metals: London, 1962.
- (12) Pearson, W. B. The Crystal Chemistry and Physics of Metals and Alloys; Wiley-Interscience: New York, 1972.
- (13) Simon, A. Intermetallic Compounds and the Use of Atomic Radii in Their Description. *Angew. Chem., Int. Ed. Engl.* **1983**, 22, 95–113
- (14) Amerioun, S.; Häussermann, U. Structure and Bonding of Sr₃In₁₁: How Size and Electronic Effects Determine Structural Stability of Polar Intermetallic Compounds. *Inorg. Chem.* **2003**, 42, 7782–7788.
- (15) Gómez, C. P.; Lidin, S. Superstructure of Eu₄Cd₂₅: A Quasicrystal Approximant. *Chem. Eur. J.* **2004**, *10*, 3279–3285.
- (16) Xia, S.-Q.; Bobev, S. Interplay between Size and Electronic Effects in Determining the Homogeneity Range of the $A_9Zn_{4+x}Pn_9$ and $A_9Cd_{4+x}Pn_9$ Phases (0 $\leq x \leq$ 0.5), A = Ca, Sr, Yb, Eu; Pn = Sb, Bi. *J. Am. Chem. Soc.* **2007**, 129, 10011–10018.
- (17) Fredrickson, D. C.; Lidin, S.; Venturini, G.; Malaman, B.; Christensen, J. Origins of Superstructure Ordering and Incommensurability in Stuffed CoSn-Type Phases. *J. Am. Chem. Soc.* **2008**, *130*, 8195–8214.
- (18) Wang, F.; Miller, G. J. Revisiting the Zintl-Klemm Concept: Alkali Metal Trielides. *Inorg. Chem.* **2011**, *50*, 7625–7636.
- (19) Oliynyk, A. O.; Stoyko, S. S.; Mar, A. Many Metals Make the Cut: Quaternary Rare-Earth Germanides RE₄M₂InGe₄ (M = Fe, Co, Ni, Ru, Rh, Ir) and RE₄RhInGe₄ Derived from Excision of Slabs in RE₂InGe₂. *Inorg. Chem.* **2015**, *54*, 2780–2792.
- (20) Engelkemier, J.; Green, L. M.; McDougald, R. N.; McCandless, G. T.; Chan, J. Y.; Fredrickson, D. C. Putting ScTGa₅ (T = Fe, Co, Ni) on the Map: How Electron Counts and Chemical Pressure Shape the Stability Range of the HoCoGa₅ Type. *Cryst. Growth Des.* **2016**, 16, 5349–5358.
- (21) Tan, X.; Tener, Z. P.; Shatruk, M. Correlating Itinerant Magnetism in RCo_2Pn_2 Pnictides (R = La, Ce, Pr, Nd, Eu, Ca; Pn = P, As) to Their Crystal and Electronic Structures. *Acc. Chem. Res.* **2018**, *51*, 230–239.
- (22) Filippetti, A.; Fiorentini, V. Theory and Applications of the Stress Density. *Phys. Rev. B: Condens. Matter Mater. Phys.* **2000**, *61*, 8433–8442.
- (23) Rogers, C. L.; Rappe, A. M. Geometric Formulation of Quantum Stress Fields. *Phys. Rev. B: Condens. Matter Mater. Phys.* **2002**, *65*, 224117.
- (24) Godfrey, M. J. Stress Field in Quantum Systems. *Phys. Rev. B: Condens. Matter Mater. Phys.* **1988**, *37*, 10176–10183.
- (25) Nielsen, O. H.; Martin, R. M. Quantum-Mechanical Theory of Stress and Force. *Phys. Rev. B: Condens. Matter Mater. Phys.* **1985**, *32*, 3780–3791.
- (26) Ziesche, P.; Gräfenstein, J.; Nielsen, O. H. Quantum-Mechanical Stress and a Generalized Virial Theorem for Clusters and Solids. *Phys. Rev. B: Condens. Matter Mater. Phys.* **1988**, 37, 8167–8178.
- (27) Fredrickson, D. C. Electronic Packing Frustration in Complex Intermetallic Structures: The Role of Chemical Pressure in Ca₂Ag₇. *J. Am. Chem. Soc.* **2011**, *133*, 10070–10073.

- (28) Fredrickson, D. C. DFT-Chemical Pressure Analysis: Visualizing the Role of Atomic Size in Shaping the Structures of Inorganic Materials. *J. Am. Chem. Soc.* **2012**, *134*, 5991–5999.
- (29) Engelkemier, J.; Berns, V. M.; Fredrickson, D. C. First-Principles Elucidation of Atomic Size Effects Using DFT-Chemical Pressure Analysis: Origins of Ca₃₆Sn₂₃'s Long-Period Superstructure. *J. Chem. Theory Comput.* **2013**, *9*, 3170–3180.
- (30) Berns, V. M.; Engelkemier, J.; Guo, Y.; Kilduff, B. J.; Fredrickson, D. C. Progress in Visualizing Atomic Size Effects with DFT-Chemical Pressure Analysis: From Isolated Atoms to Trends in AB₅ Intermetallics. *J. Chem. Theory Comput.* **2014**, *10*, 3380–3392.
- (31) Engelkemier, J.; Fredrickson, D. C. Chemical Pressure Schemes for the Prediction of Soft Phonon Modes: A Chemist's Guide to the Vibrations of Solid State Materials. *Chem. Mater.* **2016**, *28*, 3171–3183.
- (32) Berns, V. M.; Fredrickson, D. C. Problem Solving with Pentagons: Tsai-Type Quasicrystal as a Structural Response to Chemical Pressure. *Inorg. Chem.* **2013**, *52*, 12875–12877.
- (33) Hilleke, K. P.; Fredrickson, R. T.; Vinokur, A. I.; Fredrickson, D. C. Substitution Patterns Understood through Chemical Pressure Analysis: Atom/Dumbbell and Ru/Co Ordering in Derivatives of YCo₅. Cryst. Growth Des. **2017**, 17, 1610–1619.
- (34) Kilduff, B. J.; Fredrickson, D. C. Chemical Pressure-Driven Incommensurability in CaPd₅: Clues to High-Pressure Chemistry Offered by Complex Intermetallics. *Inorg. Chem.* **2016**, *55*, 6781–6793.
- (35) Fredrickson, R. T.; Guo, Y.; Fredrickson, D. C. Epitaxial Stabilization between Intermetallic and Carbide Domains in the Structures of Mn₁₆SiC₄ and Mn₁₇Si₂C₄. *J. Am. Chem. Soc.* **2016**, *138*, 248–256.
- (36) Guo, Y.; Fredrickson, D. C. On the Functionality of Complex Intermetallics: Frustration, Chemical Pressure Relief, and Potential Rattling Atoms in Y₁₁Ni₆₀C₆. *Inorg. Chem.* **2016**, *55*, 10397–10405.
- (37) Hadler, A. B.; Harris, N. A.; Fredrickson, D. C. New Roles for Icosahedral Clusters in Intermetallic Phases: Micelle-like Segregation of Ca–Cd and Cu–Cd Interactions in Ca₁₀Cd₂₇Cu₂. *J. Am. Chem. Soc.* **2013**, *135*, 17369–17378.
- (38) Hafner, J. Charge-density analysis of bonding in Laves phases. J. Phys. F: Met. Phys. 1985, 15, 1879–1893.
- (39) Häussermann, U.; Wengert, S.; Hofmann, P.; Savin, A.; Jepsen, O.; Nesper, R. Localization of Electrons in Intermetallic Phases Containing Aluminum. *Angew. Chem., Int. Ed. Engl.* **1994**, 33, 2069–2073
- (40) Amerioun, S.; Simak, S. I.; Häussermann, U. Laves-Phase Structural Changes in the System CaAl_{2-x}Mg_x. *Inorg. Chem.* **2003**, 42, 1467–1474.
- (41) Amerioun, S.; Yokosawa, T.; Lidin, S.; Häussermann, U. Phase Stability in the Systems $AeAl_{2-x}Mg_x$ (Ae = Ca, Sr, Ba): Electron Concentration and Size Controlled Variations on the Laves Phase Structural Theme. *Inorg. Chem.* **2004**, *43*, 4751–4760.
- (42) Nesper, R.; Miller, G. J. A Covalent View of Chemical Bonding in Laves Phases CaLi_xAl_{2-x}. *J. Alloys Compd.* **1993**, *197*, 109–121.
- (43) Kal, S.; Stoyanov, E.; Belieres, J.-P.; Groy, T. L.; Norrestam, R.; Häussermann, U. High-pressure modifications of CaZn₂, SrZn₂, SrAl₂, and BaAl₂: Implications for Laves phase structural trends. *J. Solid State Chem.* **2008**, *181*, 3016–3023.
- (44) Söderberg, K.; Boström, M.; Kubota, Y.; Nishimatsu, T.; Niewa, R.; Häussermann, U.; Grin, Y.; Terasaki, O. Crystal Structures and Phase Stability in Pseudobinary CaAl_{2-x}Zn_x. *J. Solid State Chem.* **2006**, 179, 2690–2697.
- (45) Gomes de Mesquita, A. H.; Buschow, K. H. J. The Crystal Structure of So-Called α -LaAl₄ (La₃Al₁₁). *Acta Crystallogr.* **1967**, 22, 497–501.
- (46) Gonze, X.; Beuken, J. M.; Caracas, R.; Detraux, F.; Fuchs, M.; Rignanese, G. M.; Sindic, L.; Verstraete, M.; Zerah, G.; Jollet, F.; et al. First-Principles Computation of Material Properties: the ABINIT Software Project. *Comput. Mater. Sci.* **2002**, *25*, 478–492.
- (47) Gonze, X. A Brief Introduction to the ABINIT Software Package. Z. Kristallogr. Cryst. Mater. 2005, 220, 558-562.

- (48) Gonze, X.; Amadon, B.; Anglade, P. M.; Beuken, J. M.; Bottin, F.; Boulanger, P.; Bruneval, F.; Caliste, D.; Caracas, R.; Côté, M.; et al. ABINIT: First-Principles Approach to Material and Nanosystem Properties. *Comput. Phys. Commun.* **2009**, *180*, 2582–2615.
- (49) Gonze, X.; Jollet, F.; Abreu Araujo, F.; Adams, D.; Amadon, B.; Applencourt, T.; Audouze, C.; Beuken, J. M.; Bieder, J.; Bokhanchuk, A.; et al. Recent Developments in the ABINIT Software Package. Comput. Phys. Commun. 2016, 205, 106–131.
- (50) Hartwigsen, C.; Goedecker, S.; Hutter, J. Relativistic Separable Dual-Space Gaussian Pseudopotentials from H to Rn. *Phys. Rev. B: Condens. Matter Mater. Phys.* **1998**, *58*, 3641–3662.
- (51) Gonze, X.; Lee, C. Dynamical Matrices, Born Effective Charges, Dielectric Permittivity Tensors, and Interatomic Force Constants from Density-Functional Perturbation Theory. *Phys. Rev. B: Condens. Matter Mater. Phys.* **1997**, *55*, 10355–10368.
- (52) Gonze, X. First-Principles Responses of Solids to Atomic Displacements and Homogeneous Electric Fields: Implementation of a Conjugate-Gradient Algorithm. *Phys. Rev. B: Condens. Matter Mater. Phys.* 1997, 55, 10337–10354.
- (53) Kresse, G.; Furthmüller, J. Efficient Iterative Schemes for ab initio Total-Energy Calculations Using a Plane-Wave Basis Set. *Phys. Rev. B: Condens. Matter Mater. Phys.* **1996**, *54*, 11169–11186.
- (54) Kresse, G.; Furthmüller, J. Efficiency of ab-initio Total Energy Calculations for Metals and Semiconductors Using a Plane-Wave Basis Set. *Comput. Mater. Sci.* **1996**, *6*, 15–50.
- (55) Blöchl, P. E. Projector Augmented-Wave Method. Phys. Rev. B: Condens. Matter Mater. Phys. 1994, 50, 17953-17979.
- (56) Kresse, G.; Joubert, D. From Ultrasoft Pseudopotentials to the Projector Augmented-Wave Method. *Phys. Rev. B: Condens. Matter Mater. Phys.* **1999**, *59*, 1758–1775.
- (57) Henkelman, G.; Arnaldsson, A.; Jónsson, H. A Fast and Robust Algorithm for Bader Decomposition of Charge Density. *Comput. Mater. Sci.* **2006**, *36*, 354–360.
- (58) Sanville, E.; Kenny, S. D.; Smith, R.; Henkelman, G. Improved Grid-Based Algorithm for Bader Charge Allocation. *J. Comput. Chem.* **2007**, 28, 899–908.
- (59) Tang, W.; Sanville, E.; Henkelman, G. A Grid-Based Bader Analysis Algorithm without Lattice Bias. *J. Phys.: Condens. Matter* **2009**, 21, 084204.
- (60) Similar atomic charges are obtained when using PAW-LDA potentials (though with a tendency for slightly smaller magnitudes) for the VASP calculations to give electronic structures more closely analogous to those of the ABINIT calculations. See the Supporting Information for plots of the Bader charges.
- (61) Oliveira, M. J. T.; Nogueira, F. Generating Relativistic Pseudopotentials with Explicit Incorporation of Semi-Core States Using APE, the Atomic Pseudo-potentials Engine. *Comput. Phys. Commun.* **2008**, 178, 524–534.
- (62) Martin, R. M. Electronic Structure: Basic Theory and Practical Methods; Cambridge University Press: Cambridge, U.K., 2008.
- (63) Hirshfeld, F. L. Bonded-Atom Fragments for Describing Molecular Charge Densities. *Theoret. Chim. Acta* 1977, 44, 129–138. (64) Segall, B. Energy Bands of Aluminum. *Phys. Rev.* 1961, 124,
- (64) Segall, B. Energy Bands of Aluminum. *Phys. Rev.* **1961**, 124 1797–1806.
- (6S) Born, M.; Huang, K. Dynamical Theory of Crystal Lattices; Clarendon Press: Oxford, U.K., 1954.
- (66) Ewald, P. P. Die Berechnung optischer und elektrostatischer Gitterpotentiale. *Ann. Phys.* **1921**, *369*, 253–287.
- (67) Pearson, W. B. Laves Structures, MgCu₂, MgZn₂, MgNi₂. Acta Crystallogr., Sect. B: Struct. Crystallogr. Cryst. Chem. **1968**, 24, 7–9.
- (68) Pearson, W. B. The Geometrical Factor in the Crystal Chemistry of Metals: Near-Neighbour Diagrams. *Acta Crystallogr., Sect. B: Struct. Crystallogr. Cryst. Chem.* **1968**, 24, 1415–1422.
- (69) Pearson, W. B. Dimensional Analysis of Laves Phases: Phases with the MgCu₂ Structure. *Acta Crystallogr., Sect. B: Struct. Crystallogr. Cryst. Chem.* **1981**, *37*, 1174–1183.
- (70) Brauer, G. The crystal structure of TiAl₃, CbAl₃, TaAl₃ and ZrAl₃. Z. Anorg. Allg. Chem. 1939, 242, 1-22.

- (71) Lee, C.-S.; Miller, G. J. Where Are the Elements in Complex Aluminides? An Experimental and Theoretical Investigation of the Quasicrystalline Approximants, Mg_{2-y}(Zn_xAl_{1-x})_{3+y}. J. Am. Chem. Soc. **2000**, 122, 4937–4947.
- (72) Steurer, W. Twenty Years of Structure Research on Quasicrystals. Part I. Pentagonal, Octagonal, Decagonal and Dodecagonal Quasicrystals. Z. Kristallogr. Cryst. Mater. 2004, 219, 391–446.
- (73) Conrad, M.; Harbrecht, B.; Weber, T.; Jung, D. Y.; Steurer, W. Large, Larger, Largest–A Family of Cluster-based Tantalum Copper Aluminides with Giant Unit Cells. II. The Cluster Structure. *Acta Crystallogr., Sect. B: Struct. Sci.* **2009**, *65*, 318–325.
- (74) Bruzzone, G.; Fornasini, M. L.; Merlo, F. Re-examination of the Ca-Ga System and Crystal Structure of CaGa₄, a Monoclinic Distortion of the BaAl₄ type. *J. Less-Common Met.* **1989**, *154*, *67*–77.
- (75) Häussermann, U.; Amerioun, S.; Eriksson, L.; Lee, C.-S.; Miller, G. J. The s-p Bonded Representatives of the Prominent BaAl₄ Structure Type: A Case Study on Structural Stability of Polar Intermetallic Network Structures. *J. Am. Chem. Soc.* **2002**, *124*, 4371–4383
- (76) Gout, D.; Barker, T. J.; Gourdon, O.; Miller, G. J. A New Superstructure for the BaAl₄-Structure Type: An Experimental and Theoretical Study of La₂NiAl₂. *Chem. Mater.* **2005**, *17*, 3661–3667.
- (77) Suen, N.-T.; Bobev, S. Synthesis and Structural Characterization of $RE_7Zn_{21}Tt_2$ (RE = La–Nd; Tt = Ge, Sn, and Pb): New Structure Type Among the Polar Intermetallic Phases. *Inorg. Chem.* **2013**, *52*, 12731–12740.
- (78) Han, M.-K.; Morosan, E.; Canfield, P. C.; Miller, G. J. The Coloring Problem in Intermetallics: Bonding and Properties of ${\rm Tb_3Zn_{3.6}Al_{7.4}}$ with the ${\rm La_3Al_{11}}$ Structure Type. Z. Kristallogr. Cryst. Mater. 2005, 220, 95.
- (79) Pöttgen, R. $Dy_3Co_6Sn_5 a$ New Stannide with an Ordered La_3Al_{11} Type Structure. Z. Naturforsch., B: J. Chem. Sci. **1995**, 50, 175.
- (80) Subbarao, U.; Roy, S.; Sarma, S. C.; Sarkar, S.; Mishra, V.; Khulbe, Y.; Peter, S. C. Metal Flux Growth, Structural Relations, and Physical Properties of $EuCu_2Ge_2$ and $Eu_3T_2In_9$ (T = Cu and Ag). *Inorg. Chem.* **2016**, *55*, 10351–10360.
- (81) Speka, M.; Prots, Y.; Belyavina, N.; Markiv, V. Y.; Grin, Y. Crystal Structure of Yttrium Copper Gallide, Y₃Cu₄Ga₇. Z. Kristallogr. New Cryst. Struct. **2004**, 219, 211–212.
- (82) Mao, J.-G.; Guloy, A. M. Synthesis, Structure and Properties of Sr₃In₁₁—Optimizing the Chemical Bonding of Hypoelectronic SrIn₄. *J. Alloys Compd.* **2004**, 363, 143–149.